DRAFT VERSION DECEMBER 3, 2019
Typeset using LATEX default style in AASTeX62

Spitzer + VLTI-GRAVITY Measure the Lens Mass of a Nearby Microlensing Event

WEICHENG ZANG,[1] SUBO DONG,[2] ANDREW GOULD,[3,4] SEBASTIANO CALCHI NOVATI,[5] PING CHEN,[2,6] HONGJING YANG,[1]
SHUN-SHENG LI,[7,8] SHUDE MAO,[1,7] K.B. ALTON,[9] J. BRIMACOMBE,[10] SEAN CAREY,[11] G. W. CHRISTIE,[12]
F. DELPLANCKE-STRÖBELE,[13] DAX L. FELIZ,[14] J. GREEN,[15] SHAOMING HU,[16] T. JAYASINGHE,[17,18] R. A. KOFF,[19] A. KURTENKOV,[20]
A. MÉRAND,[13] MILEN MINEV,[21] ROBERT MUTEL,[22] T. NATUSCH,[23] TYLER ROTH,[22] YOSSI SHVARTZVALD,[24] FENGWU SUN,[25]
T. VANMUNSTER,[26] AND WEI ZHU[27]

[1]*Department of Astronomy and Tsinghua Centre for Astrophysics, Tsinghua University, Beijing 100084, China*
[2]*Kavli Institute for Astronomy and Astrophysics, Peking University, Yi He Yuan Road 5, Hai Dian District, Beijing 100871, China*
[3]*Max-Planck-Institute for Astronomy, Königstuhl 17, 69117 Heidelberg, Germany*
[4]*Department of Astronomy, Ohio State University, 140 W. 18th Ave., Columbus, OH 43210, USA*
[5]*IPAC, Mail Code 100-22, Caltech, 1200 E. California Blvd., Pasadena, CA 91125, USA*
[6]*Department of Astronomy, School of Physics, Peking University, Yi He Yuan Road 5, Hai Dian District, Beijing 100871, China*
[7]*National Astronomical Observatories, Chinese Academy of Sciences, Beijing 100101, China*
[8]*School of Astronomy and Space Science, University of Chinese Academy of Sciences, Beijing 100049, China*
[9]*Desert Blooms Observatory*
[10]*Coral Towers Observatory, Cairns, Queensland 4870, Australia*
[11]*Spitzer Science Center, MS 220-6, California Institute of Technology,Pasadena, CA, USA*
[12]*Auckland Observatory, Box 24180, Auckland, New Zealand*
[13]*European Southern Observatory, Karl-Schwarzschild-Str. 2, 85748 Garching, Germany*
[14]*Department of Physics and Astronomy, Vanderbilt University, Nashville, TN 37235, USA*
[15]*Kumeu Observatory, Kumeu, New Zealand*
[16]*Shandong Provincial Key Laboratory of Optical Astronomy and Solar-Terrestrial Environment, Institute of Space Sciences, Shandong University, Weihai
264209, People's Republic of China*
[17]*Department of Astronomy Ohio State University, 140 W. 18th Ave., Columbus, OH 43210, USA*
[18]*Center for Cosmology and AstroParticle Physics (CCAPP), The Ohio State University, 191 W. Woodruff Avenue, Columbus, OH 43210, USA.*
[19]*Antelope Hills Observatory, 980 Antelope Drive West, Bennett, CO 80102, USA*
[20]*Institute of Astronomy and National Astronomical Observatory, Bulgarian Academy of Sciences, 72 Tsarigradsko Shose Blvd., 1784 Sofia, Bulgaria*
[21]*Department of Astronomy, Faculty of Physics, University of Sofia, 1164 Sofia, Bulgaria*
[22]*Department of Physics and Astronomy, University of Iowa*
[23]*Institute for Radio Astronomy and Space Research, AUT University, Auckland, New Zealand*
[24]*Department of Particle Physics and Astrophysics, Weizmann Institute of Science, Rehovot 76100, Israel*
[25]*Steward Observatory, University of Arizona, 933 North Cherry Avenue, Tucson, AZ 85721, USA*
[26]*Center for Backyard Astrophysics Belgium, Walhostraat 1A, B-3401 Landen, Belgium*
[27]*Canadian Institute for Theoretical Astrophysics, University of Toronto, 60 St George Street, Toronto, ON M5S 3H8, Canada*

ABSTRACT

We report the lens mass and distance measurements of the nearby microlensing event TCP
J05074264+2447555. We measure the microlens parallax vector $\boldsymbol{\pi}_{\rm E}$ using *Spitzer* and ground-based light curves
with constraints on the direction of lens-source relative proper motion derived from Very Large Telescope Inter-
ferometer (VLTI) GRAVITY observations. Combining this $\boldsymbol{\pi}_{\rm E}$ determination with the angular Einstein radius
$\theta_{\rm E}$ measured by VLTI GRAVITY observations, we find that the lens is a star with mass $M = 0.495 \pm 0.063 \, M_{\odot}$
at a distance $D_{\rm L} = 429 \pm 21$ pc. We find that the blended light basically all comes from the lens. The lens-
source proper motion is $\mu_{\rm rel,hel} = 26.55 \pm 0.36$ mas yr^{-1}, so with currently available adaptive-optics (AO)
instruments, the lens and source can be resolved in 2021. This is the first microlensing event whose lens mass
is unambiguously measured by interferometry + satellite parallax observations, which opens a new window for
mass measurements of isolated objects such as stellar-mass black holes.

Corresponding author: Weicheng Zang, Subo Dong
zangwc17@mails.tsinghua.edu.cn, dongsubo@pku.edu.cn

1. INTRODUCTION

Gravitational microlensing offers a unique window into probing extrasolar planets beyond the snow line (Mao & Paczynski 1991; Gould & Loeb 1992; Mao 2012; Gaudi 2012) and isolated dark objects such as free-floating planets (Sumi et al. 2011; Mróz et al. 2017, 2018, 2019), brown dwarfs (Gould et al. 2009; Shvartzvald et al. 2019) and black holes (Gould 2000b; Mao et al. 2002; Bennett et al. 2002; Wyrzykowski et al. 2016). For a typical microlensing event, the only measured observable that relates to the physical properties of the lens is the Einstein timescale $t_{\rm E}$. It is a combination of the lens mass $M_{\rm L}$, the lens-source relative proper motion $\boldsymbol{\mu}_{\rm rel}$ and parallax $\pi_{\rm rel}$ by

$$t_{\rm E} = \frac{\theta_{\rm E}}{\mu_{\rm rel}}; \qquad \theta_{\rm E} = \sqrt{\kappa M_{\rm L} \pi_{\rm rel}}; \qquad \pi_{\rm rel} = \pi_{\rm L} - \pi_{\rm S}, \tag{1}$$

where $\kappa \equiv 4G/(c^2{\rm AU}) = 8.144$ mas$/M_\odot$, $\theta_{\rm E}$ is the angular Einstein radius, $\pi_{\rm L} = {\rm AU}/D_{\rm L}$ and $\pi_{\rm S} = {\rm AU}/D_{\rm S}$ are the lens and source parallax, respectively, and $D_{\rm L}$ and $D_{\rm S}$ are the lens and the source distances, respectively. Therefore, with only $t_{\rm E}$ known, the lens mass and distance cannot be unambiguously determined. By far, the most common way to break this degeneracy is to also measure the angular Einstein radius $\theta_{\rm E}$ and the microlens parallax $\boldsymbol{\pi}_{\rm E}$. For a lensing object, its mass is related to these two observables by (Gould 1992, 2000a)

$$M_{\rm L} = \frac{\theta_{\rm E}}{\kappa \pi_{\rm E}}, \tag{2}$$

and the lens-source relative proper motion and parallax by

$$\boldsymbol{\mu}_{\rm rel} = \frac{\theta_{\rm E}}{t_{\rm E}} \frac{\boldsymbol{\pi}_{\rm E}}{\pi_{\rm E}}; \qquad \pi_{\rm rel} = \theta_{\rm E} \pi_{\rm E}, \tag{3}$$

where the microlens parallax vector $\boldsymbol{\pi}_{\rm E}$ is defined by

$$\boldsymbol{\pi}_{\rm E} \equiv \frac{\pi_{\rm rel}}{\theta_{\rm E}} \frac{\boldsymbol{\mu}_{\rm rel}}{\mu_{\rm rel}}. \tag{4}$$

There are three methods to measure the microlens parallax $\pi_{\rm E}$. The first one is "orbital microlens parallax", which is due to the Earth's orbital acceleration around the Sun that introduces deviation from rectilinear motion in the lens-source relative motion (Gould 1992). However, this method is generally only feasible for events with long microlensing timescales $t_{\rm E} \gtrsim$ year$/2\pi$ (e.g., Udalski et al. 2018) and/or events produced by nearby lenses (e.g., Jung et al. 2018). The second method is "terrestrial microlens parallax" (Hardy & Walker 1995; Holz & Wald 1996), which in rare cases can be measured by a combination of simultaneous observations from well-separated ground-based telescopes (e.g., Gould et al. 2009; Yee et al. 2009). The most efficient and robust way to measure $\boldsymbol{\pi}_{\rm E}$ is via "satellite microlens parallax", which is done by observing the same microlensing event from Earth and one or more well-separated ($\sim$ AU) satellite (Refsdal 1966; Gould 1994, 1995). The first observed example applying this method was the event OGLE-2005-SMC-001 (Dong et al. 2007), in which the joint analysis of ground-based observations and *Spitzer* observations indicates that the lens is probably a halo binary. Microlens parallax measurements from two satellites (*Spitzer* and the two-wheel *Kepler* K2) have also been achieved to measure the parallax of the event OGLE-2016-BLG-0975 (Zhu et al. 2017a). Since 2014, the *Spitzer* satellite has observed about 1000 microlensing events toward the Galactic bulge (Gould et al. 2013, 2014, 2015b,a, 2016, 2018), in order to probe planets in substantially different Galactic environments (Calchi Novati et al. 2015a; Zhu et al. 2017b), and they have yielded unambiguous mass measurements for seven planetary systems (Udalski et al. 2015; Street et al. 2016; Ryu et al. 2018; Shvartzvald et al. 2017; Calchi Novati et al. 2018; Jung et al. 2019; Gould et al. 2019).

The angular Einstein radius $\theta_{\rm E}$ is generally measured via finite-source effects (Gould 1994; Witt & Mao 1994; Nemiroff & Wickramasinghe 1994) when the source transits a caustic (where the magnification diverges to infinity) or comes close to a cusp. The detection of finite-source effects usually yields the source radius normalized by the Einstein radius, ρ, and combining it with the source angular radius θ_*, which is routinely determined from the intrinsic color and de-reddened brightness of the source (Yoo et al. 2004), can lead to the measurement of the angular Einstein radius $\theta_{\rm E} = \theta_*/\rho$. Finite-source effects are frequently detected in binary/planetary events due to their relatively large caustic structures, but they are rarely measured in a single-lens event since its caustic is a single geometric point.

Besides the mass measurements from combining the angular Einstein radius $\theta_{\rm E}$ and the microlens parallax $\pi_{\rm E}$, an independent mass-distance relationship can be obtained if the flux from the lens system is measured with high angular resolution imaging and compared to stellar models (see, e.g., Bennett et al. 2007; Yee 2015). These are achieved either by measuring the flux at the position of the source star in excess of the source flux to constrain the lens flux (e.g., Koshimoto et al. 2017a,b), or in some cases,

resolving the source and lens $\sim$ 5–20 years after the microlensing event and thus directly measure the lens flux (e.g., Alcock et al. 2001; Batista et al. 2015; Bennett et al. 2015; Bhattacharya et al. 2018). The additional mass-distance relationship from the lens flux, combined with the constraints from the angular Einstein radius $\theta_{\rm E}$ and/or the microlens parallax, can yield the mass and distance of the lens system (e.g., Dong et al. 2009; Beaulieu et al. 2018). However, this method is not feasible for dark lenses such as free-floating planets and black holes.

Here we report the lens mass measurement of the nearby microlensing event TCP J05074264+2447555 (hereafter referred to as "TCP J0507+2447" for brevity) by a joint analysis of ground-based, *Spitzer*, and VLTI GRAVITY observations of Dong et al. (2019). The paper is structured as follows. In § 2, we introduce the ground-based and *Spitzer* observations. We then describe the light curve modeling process in § 3. In § 4, we derive the physical parameters of the lens. Finally, we discuss the implications of our work in § 5.

2. OBSERVATIONS

TCP J0507+2447, at equatorial coordinates $(\alpha, \delta)_{\rm J2000} = (05:07:42.72, +24:47:56.4,$ Gaia Collaboration et al. 2018), corresponding to Galactic coordinates $(\ell, b) = (178.76, -9.33)$, was first discovered by the Japanese amateur astronomer Tadashi Kojima (Gunma-ken, Japan) on UT 2017-10-25.688. For ground-based data, we choose the light curves used by Dong et al. (2019), including the data from All-Sky Automatic Survey for Supernovae (ASAS-SN; Shappee et al. 2014), 0.6 m telescopes at Post Observatory (RP), 0.5 m Iowa Robotic Telescope (Iowa) at the Winer Observatory (Arizona, USA), 0.4m telescope at Auckland Observatory (AO), and the 1.3m SMARTS telescope (DePoy et al. 2003) at Cerro Tololo Inter-American Observatory (CTIO). We supplement it with CTIO V-band data to derive the VHL color-color relation. All the ground-based data were calibrated to standard magnitude systems. For further descriptions of our ground-based data and their availability in digital format, see Appendix § B.

For *Spitzer*, we submitted a Director Discretion Time (DDT) proposal (Dong et al. 2017) to observe the TCP J0507+2447 on 2017 November 7, and it was approved on 2017 November 9. Due to the Sun-angle limit, it did not start taking observations until 2017 December 19 ($\rm HJD' = 8107.2, HJD' = HJD - 2450000$). The observations ended on 2018 January 23 ($\rm HJD' = 8143.7$). In total, 21 data points were taken, all using the 3.6 μm channel ($L-$band) of the IRAC camera. The data were reduced by the method presented by Calchi Novati et al. (2015b).

3. LIGHT CURVE ANALYSIS

Figure 1 shows the TCP J0507+2447 data together with the best-fit single-lens model. In this section, we analyze the data with a single-lens model. Nucita et al. (2018) reported a short-duration planetary anomaly near the peak of the event, and we discuss the planetary-lens modeling in Appendix§ A, in order to double check whether the measurements of the microlens parallax $\pi_{\rm E}$ is affected by the planetary model.

3.1. *Ground-based data only*

The single-lens model has three parameters t_0, u_0, $t_{\rm E}$ (Paczyński 1986) to calculate the magnification as a function of time $A(t)$: the time of the maximum magnification t_0, the impact parameter u_0 (in units of the angular Einstein radius $\theta_{\rm E}$), and the Einstein radius crossing time $t_{\rm E}$. For each data set i, we introduce two flux parameters $(f_{{\rm S},i}, f_{{\rm B},i})$ in order to model the observed flux $f_i(t)$ as

$$f_i(t) = f_{{\rm S},i} A(t) + f_{{\rm B},i}, \tag{5}$$

where $f_{{\rm S},i}$ represents the flux of the source star, and $f_{{\rm B},i}$ represents any blended flux that is not lensed in the photometric aperture. In addition, to fit the orbital microlens parallax, we parameterize the microlens parallax effects by $\pi_{\rm E,N}$ and $\pi_{\rm E,E}$, which are the North and East components of the microlens parallax vector (Gould 2004), respectively. We also fit $u_{0,\oplus} > 0$ and $u_{0,\oplus} < 0$ solutions to consider the "ecliptic degeneracy" (Jiang et al. 2004; Poindexter et al. 2005). We find $\pi_{\rm E} = 0.13 \pm 0.47$ for the $u_{0,\oplus} > 0$ solution and $\pi_{\rm E} = 0.67 \pm 0.52$ for the $u_{0,\oplus} < 0$ solution. The likelihood distributions of $(\pi_{\rm E,N}, \pi_{\rm E,E})$ from ground-based data are shown in Figure 2.

3.2. *Satellite parallax*

For TCP J0507+2447, *Spitzer* took observations in $1.7 < (t - t_{0,\oplus})/t_{\rm E} < 3.1$. We can estimate the microlens parallax by

$$\vec{\pi}_{\rm E} \sim \frac{\rm au}{D_\perp}(\Delta\tau, \Delta\beta), \qquad \Delta\tau \equiv \frac{t_{0,Spitzer} - t_{0,\oplus}}{t_{\rm E}}, \qquad \Delta\beta \equiv \pm u_{0,Spitzer} - \pm u_{0,\oplus}, \tag{6}$$

where $D_\perp$ is the projected separation between the *Spitzer* satellite[1] and Earth at the time of the event. Generally, the four possible values of $\Delta\beta$ result in a set of four degenerate solutions (Refsdal 1966; see also Figure 1 from Gould 1994). However, the four solutions merge into two disjoint ($u_{0,\oplus} > 0$ and $u_{0,\oplus} < 0$) solutions because the *Spitzer* data commence well after $t_{0,Spitzer}$ (Gould 2019). In addition, we include a VHL color-color constraint on the *Spitzer* source flux $f_{s,Spitzer}$ (e.g., Calchi Novati et al. 2015a), which adds a χ^2_{Color} into the total χ^2_{total},

$$\chi^2_{\text{Color}} = \frac{[(V-L)_{\text{S}} - (V-L)_{\text{fix}}]^2}{\sigma^2_{\text{cc}}}, \tag{7}$$

where $(V-L)_{\text{S}}$ is the source color from the modeling, $(V-L)_{\text{fix}}$ is the color constraint, and σ_{cc} is the uncertainty of the color constraint. To derive the color constraint, we extract the CTIO V- and H- band and *Spitzer* L-band photometry for stars within $1'$ (10 stars in total), and fit for the two parameters c_0 and c_1 in the equation

$$V_{\text{CTIO}} - L_{Spitzer} = c_0 + c_1(V_{\text{CTIO}} - H_{\text{CTIO}} - X_p), \tag{8}$$

where $X_p = 3.14$ is a pivot parameter chosen to minimize the covariance between c_0 and c_1. We get $c_0 = 2.370 \pm 0.016, c_1 = 0.988 \pm 0.043$. We derive the source color by regression of CTIO V versus H flux as the source magnification changes, and find $(V_{\text{CTIO}} - H_{\text{CTIO}})_{\text{S}} = 2.096 \pm 0.024, (V-L)_{\text{fix}} = 1.34 \pm 0.06$. We apply the color constraint to the modeling and find $\pi_{\text{E}} = 0.68 \pm 0.23$ for the $u_{0,\oplus} > 0$ solution and $\pi_{\text{E}} = 1.01 \pm 0.34$ for the $u_{0,\oplus} < 0$ solution.

The measured satellite parallax above is a combination of orbital parallax and satellite parallax. To investigate the satellite parallax from the *Spitzer* data, we fix $(t_0, u_{0,\oplus}, t_{\text{E}})$ from the best-fit non-parallax model, and fit the parallax only with *Spitzer* data and the color constraint. We find the resulting "Ground + *Spitzer*" parallax is an intersection of the satellite parallax, which is nearly a circle, and the orbital parallax, which is nearly a straight line. Gould (2019) shows that the nearly circular shape of the satellite-parallax contours are due to partial overlap of a series of osculating, exactly circular, degeneracies in the π_{E} plane, and similar satellite-parallax shapes have been detected in two *Spitzer* planetary events (Jung et al. 2019; Gould et al. 2019). The best-fit parameters for the $u_{0,\oplus} > 0$ and $u_{0,\oplus} < 0$ solutions are shown in Tables 2 and 3, respectively. The likelihood distributions of $(\pi_{\text{E,N}}, \pi_{\text{E,E}})$ from "*Spitzer*-only" and "Ground + *Spitzer*" are shown in Figure 2.

3.3. *VLTI constraint on the parallax direction*

VLTI GRAVITY provides constraints on the direction of the lens-source relative proper motion and thus (see Equation 4) the direction of the microlens parallax (see Figure 4 of Dong et al. 2019). For the "no lens light" model, the direction of the microlens parallax (North through East)

$$\Phi_{\text{VLTI}} = \begin{cases} 192.9° \pm 0.4° & \text{for } u_{0,\oplus} < 0 \tag{9} \\ 156.1° \pm 0.4° & \text{for } u_{0,\oplus} > 0, \tag{10} \end{cases}$$

and for the "luminous lens " model,

$$\Phi_{\text{VLTI}} = \begin{cases} 193.5° \pm 0.4° & \text{for } u_{0,\oplus} < 0 \tag{11} \\ 156.7° \pm 0.4° & \text{for } u_{0,\oplus} > 0. \tag{12} \end{cases}$$

We include the constraint of the parallax direction by adding a χ^2_{VLTI} into the total χ^2_{total},

$$\chi^2_{\text{VLTI}} = \frac{(\Phi_{\text{model}} - \Phi_{\text{VLTI}})^2}{\sigma^2_{\text{VLTI}}}, \tag{13}$$

where Φ_{VLTI} is the parallax direction from the modeling, and $\sigma_{\text{VLTI}} = 0.4°$ is the uncertainty of the VLTI parallax direction. The best-fit parameters are shown in Tables 2 and 3, and its likelihood distributions of $(\pi_{\text{E,N}}, \pi_{\text{E,E}})$ are shown in Figure 3. For both the "no lens light" model and the "luminous lens" model, the $u_{0,\oplus} < 0$ solution is disfavored by $\Delta\chi^2 > 41$. Actually, from the likelihood distributions of $(\pi_{\text{E,N}}, \pi_{\text{E,E}})$ from "Ground + *Spitzer*" data shown in Figure 2, we can see that the VLTI parallax direction for the $u_{0,\oplus} < 0$ solution is inconsistent with the constraint from the "Ground + *Spitzer*" data. Thus, we reject the $u_{0,\oplus} < 0$ solution.

---

[1] We extract the geocentric locations of *Spitzer* from the *JPL Horizons* website: http://ssd.jpl.nasa.gov/?horizons

4. PHYSICAL PARAMETERS

4.1. *Is the lens luminous?*

For the "no lens light" model, VLTI measured the angular Einstein radius $\theta_{\rm E} = 1.850 \pm 0.014$ mas, and the light curve modeling shows $\pi_{\rm E} = 0.476 \pm 0.061$, so the lens mass $M_{\rm L} = 0.477 \pm 0.061 M_{\odot}$ and the lens source relative parallax $\pi_{\rm rel} = \theta_{\rm E}\pi_{\rm E} = 0.880 \pm 0.113$ mas. The parallax of the "baseline object" has been measured by *Gaia* second data release (DR2) (Gaia Collaboration et al. 2018; Bailer-Jones et al. 2018)

$$\pi_{\rm base} = 1.480 \pm 0.031 \text{ mas} \tag{14}$$

which is the flux-weighted mean parallax of the source and the blend in *Gaia* band,

$$\pi_{\rm base} = \eta\pi_{\rm B} + (1 - \eta)\pi_{\rm S}, \tag{15}$$

where η is the fraction of total *Gaia* flux due to the blending, $\pi_{\rm B}$ is the parallax of the blending. The *Gaia* band is qualitatively similar to V band, and the best-fit solution of the "no lens light" model has $f_{{\rm B},V}/f_{{\rm S},V} \sim 0.04$, so we estimate $\pi_{\rm S} \sim \pi_{\rm base}$, and $D_{\rm L} = {\rm AU}/(\pi_{\rm rel} + \pi_{\rm S}) = 424 \pm 14$ pc. Using the MIST isochrones[2] with age $\geq$ 2Gyr, the lens has an absolute K-band magnitude of $K_{\rm L,0} = 5.7 \pm 0.3$. Dong et al. (2019) has found that the source suffers from an extinction $A_{K,{\rm S}} = 0.155$, we thus estimate the extinction of the lens $A_{K,{\rm L}} \sim A_{K,{\rm S}}D_{\rm L}/D_{\rm S} = 0.097$. As a result, the apparent K-band magnitude of the lens is

$$K_{\rm L} = K_{\rm L,0} + 5\log\frac{D_{\rm L}}{10 \text{ pc}} + A_{K,{\rm L}} = 13.9 \pm 0.3, \tag{16}$$

which is $\sim 13\%$ of the 2MASS baseline $K = 11.680 \pm 0.018$. Thus, the lens is luminous, and we reject the "no lens light" model.

4.2. *Blend = Lens?*

Table 4 shows the blend in H-, I-, R-, V- bands from the best-fit "luminous lens" model, which shows that the blend is detected in all bands. To estimate the lens apparent brightness, we use the angular Einstein radius $\theta_{\rm E} = 1.891 \pm 0.014$ mas and $\pi_{\rm E} = 0.469 \pm 0.060$ of the "luminous lens" model, and follow the procedure in Section 4.1. For extinction, we adopt the extinction law of Cardelli et al. (1989) and estimate the extinction of the lens in λ band $A_{\lambda,{\rm L}} \sim A_{\lambda,{\rm S}}D_{\rm L}/D_{\rm S}$. The predicted lens apparent magnitude is shown in Table 4. We find that the predicted lens apparent magnitude is consistent with the blend within 1σ in all bands. Thus, the blended light basically all comes from the lens.

4.3. *Lens parameters*

According to the best-fit "luminous lens" model, the lens mass

$$M = \frac{\theta_{\rm E}}{\kappa\pi_{\rm E}} = 0.495 \pm 0.063 \ M_{\odot}, \tag{17}$$

the lens-source relative parallax

$$\pi_{\rm rel} = \theta_{\rm E}\pi_{\rm E} = 0.887 \pm 0.114 \text{ mas}. \tag{18}$$

Combining Equations (1), (14) and (15), we obtain

$$\pi_{\rm L} = \pi_{\rm base} + (1 - \eta)\pi_{\rm rel} = 2.332 \pm 0.114 \text{ mas}; \qquad D_{\rm L} = \frac{{\rm AU}}{\pi_{\rm L}} = 429 \pm 21 \text{ pc}, \tag{19}$$

where we adopt $\eta = f_{{\rm B},V}/(f_{{\rm S},V} + f_{{\rm B},V}) = 0.040 \pm 0.016$ from the best-fit "luminous lens" model as the fraction of total *Gaia* flux due to the lens. The geocentric and heliocentric relative proper motion are

$$\boldsymbol{\mu}_{\rm rel,geo}(N, E) = \frac{\theta_{\rm E}}{t_{\rm E}}\frac{\boldsymbol{\pi}_{\rm E}}{\pi_{\rm E}} = (-22.73, 9.83) \pm (0.21, 0.19) \text{ mas yr}^{-1}; \tag{20}$$

$$\boldsymbol{\mu}_{\rm rel,hel}(N, E) = \boldsymbol{\mu}_{\rm rel,geo} + \frac{\pi_{\rm rel}}{{\rm AU}}\boldsymbol{v}_{\oplus,\perp} = (-22.45, 14.18) \pm (0.21, 0.59) \text{ mas yr}^{-1}, \tag{21}$$

---

[2] http://waps.cfa.harvard.edu/MIST/interpisos.html

where $\boldsymbol{v}_{\oplus,\perp} = (1.47, 23.29)$ km s^{-1} is Earth's projected velocity on the event at t_0. The proper motion of the "baseline object" has been measured by *Gaia*

$$\boldsymbol{\mu}_{\mathrm{base}}(N, E) = (-7.330, -0.228) \pm (0.033, 0.061) \mathrm{\, mas \, yr}^{-1}, \tag{22}$$

which is also the flux-weighted mean proper motion. Thus, the lens and source proper motion are

$$\boldsymbol{\mu}_{\mathrm{L}}(N, E) = \boldsymbol{\mu}_{\mathrm{base}} + (1 - \eta)\boldsymbol{\mu}_{\mathbf{rel,hel}} = (-28.89, 13.39) \pm (0.41, 0.61) \mathrm{\, mas \, yr}^{-1}; \tag{23}$$

$$\boldsymbol{\mu}_{\mathrm{S}}(N, E) = \boldsymbol{\mu}_{\mathrm{base}} - \eta\boldsymbol{\mu}_{\mathbf{rel,hel}} = (-6.43, -0.80) \pm (0.36, 0.23) \mathrm{\, mas \, yr}^{-1}. \tag{24}$$

We summarize the derived lens parameters in Table 5.

5. DISCUSSION AND CONCLUSION

We have reported the analysis of the microlensing event TCP J0507+2447. The combination of the angular Einstein radius θ_{E} measured by VLTI GRAVITY observations, and the direction of microlens parallax $\boldsymbol{\pi}_{\mathrm{E}}$ constrained from VLTI GRAVITY observations, *Spitzer* observations and ground-based observations, reveals that the lens is a $M_{\mathrm{L}} = 0.495 \pm 0.063 \, M_\odot$ star at $D_{\mathrm{L}} = 429 \pm 21$ pc. We also note that Fukui et al. (2019) reported the lens mass and distance of TCP J0507+2447 to be $M_{\mathrm{L}} = 0.581 \pm 0.033 \, M_\odot$ star at $D_{\mathrm{L}} = 505 \pm 47$ pc, which is a combination of finite-source effects, Keck AO image, spectroscopy, annual parallax and VLTI observations (see Table 4 and Figure 9 of Fukui et al. 2019). That is, their mass estimate is $1.2\,\sigma$ higher than ours. We note that Fukui et al. (2019) used spectroscopy to determine the source distance and got $D_{\mathrm{S}} = 800 \pm 130$ pc. If we adopt *Gaia* parallax, the angular Einstein radius θ_{E} measured by VLTI GRAVITY observations and the lens flux constraints of Fukui et al. (2019), we get $M_{\mathrm{L}} = 0.527 \pm 0.032 \, M_\odot$ star at $D_{\mathrm{L}} = 434 \pm 12$ pc, which is in agreement with our measurements within 1σ. Using current AO instruments, Batista et al. (2015); Bennett et al. (2015); Bhattacharya et al. (2018) resolved the lens and source for cases that these have approximately equal brightness when they were separated by 34–60 mas. In this case, the lens-source proper motion is $\mu_{\mathrm{rel,hel}} = 26.55 \pm 0.36 \mathrm{\, mas \, yr}^{-1}$, and the lens is about 1.8 mag fainter than the source in H-band. We estimate that it will probably require ~ 80 mas to resolve the source and lens. Thus, the derived physical parameters of our work can be verified by currently available AO instruments in 2021 and later.

This is the first microlensing event whose lens mass has been unambiguously measured by interferometry (VLTI GRAVITY) + satellite (*Spitzer*) parallax observations. Interferometry + satellite parallax is a new method to measure the mass of isolated objects. The detection frequency of finite-source effects in a single event is only $\sim 2\%$ (Zhu et al. 2016; Zang et al. 2019), so interferometric observation such as VLTI GRAVITY is a complementary approach to measurements of the angular Einstein radius θ_{E}. In addition, interferometry can provide additional constraints on the microlens parallax direction, which is helpful for breaking degeneracy in the parallax measuremnets (Refsdal 1966; Gould 1994). Gould (2000b) estimated that $\sim 20\%$ of Galactic microlensing events are caused by stellar remnants, and specifically that $\sim 1\%$ are due to stellar-mass black-hole lenses. Some black-hole candidates (Mao et al. 2002; Bennett et al. 2002; Wyrzykowski et al. 2016) have been reported by microlensing surveys, but none of these candidates had finite-source effects. Therefore, interferometry observations such as VLTI GRAVITY + satellite parallax opens up a new window for decisively confirming black-hole candidates by measuring their masses.

Nucita et al. (2018) reported a planetary companion in the TCP J0507+2447 lens system. Using the derived lens parameters, we infer the planet mass to be

$$M_{\mathrm{planet}} = 19.0 \pm 3.0 \, M_\oplus. \tag{25}$$

The projected planet-host separation is

$$a_\perp = s\theta_{\mathrm{E}}D_{\mathrm{L}} \begin{cases} 0.76 \pm 0.04 \mathrm{\, AU \, for \,} s \sim 0.935; & (26) \\ 0.79 \pm 0.04 \mathrm{\, AU \, for \,} s \sim 0.975, & (27) \end{cases}$$

where s is the planet-host projected separation in units of θ_{E}. Following the procedure of Han et al. (2019), we estimate the radial-velocity (RV) amplitude $v\sin(i) \sim 2.3$ m s^{-1} with a period of ~ 1.3 yr, which may be detectable by high-resolution spectrometers such as VLT/Espresso with 4 VLT telescopes. In addition, the snow line radius of the lens system is $a_{\mathrm{SL}} \sim 2.7(M/M_\odot) = 1.3$ AU (Kennedy & Kenyon 2008). Thus, this is the first Neptune within the snow line detected by microlensing.

APPENDIX

A. THE PLANETARY MODEL

Nucita et al. (2018) reported a short-duration anomaly near the peak of the event, indicating that the lens star has a planetary companion with planet-host mass ratio $q = 1.1 \times 10^{-4}$. To double check the parallax measurements, we fit the event with the binary-lens model. Besides the three parameters t_0, u_0, t_E introduced in § 3.1, the binary-lens model has four other parameters (s, q, α, ρ). Here, q is the companion-host mass ratio, s is the companion-host projected separation in units of θ_E, α is the angle between the source trajectory and the binary axis in the lens plane, and ρ is the source radius normalized to θ_E.

We fix (s, q, α) as the best-fit values shown in Nucita et al. (2018). We include the satellite parallax and the constraints from VLTI GRAVITY. We consider the so-called "minor-image perturbation degeneracy" (e.g., Koshimoto et al. 2017b; Calchi Novati et al. 2019; Han et al. 2018) found by Nucita et al. (2018): $s = 0.935 \pm 0.004$ and $s = 0.975 \pm 0.004$. Table 6 shows the best-fit parameters. For all the solutions, the resulting parallax is consistent with the results of the single-lens model within 1σ. Thus, different models (single-lens and binary-lens) do not have significant influence on the parallax and thus the mass measurements.

B. GROUND-BASED PHOTOMETRIC OBSERVATIONS

We summarize the ground-based photometric observations collected during our observing campaign in Table B. The ASCII data will be made available upon publication.

Table 1. Ground-based Photometric Observations

Site	Filter
All-Sky Automatic Survey for Supernovae (ASAS-SN)	V
Cerro Tololo Inter-American Observatory (CTIO)	V, H
Post Observatory (RP)	B, V
Auckland Observatory (AO)	R, I
Iowa Robotic Telescope (Iowa)	r, i
Desert Bloom Observatory (DBO)	B, V, I, Clear
Coral Towers Observatory (CTO)	Clear
Kumeu Observatory (KO)	Wratten12
Weihai (WH) Observatory of Shandong University	B, V
Antelope Hill Observatory (ATO)	B, V
Bulgarian National Astronomical Observatory (Rozhen)	B, V
Peking University 40cm Telescope of (PFT)	UHC
Center for Backyard Astronomy Belgium Observatory (CBABO)	V, Clear

REFERENCES

Alcock, C., Allsman, R. A., Alves, D. R., et al. 2001, Nature, 414, 617

Bailer-Jones, C. A. L., Rybizki, J., Fouesneau, M., Mantelet, G., & Andrae, R. 2018, AJ, 156, 58

Batista, V., Beaulieu, J.-P., Bennett, D. P., et al. 2015, ApJ, 808, 170

Beaulieu, J.-P., Batista, V., Bennett, D. P., et al. 2018, AJ, 155, 78

Bennett, D. P., Anderson, J., & Gaudi, B. S. 2007, ApJ, 660, 781

Bennett, D. P., Becker, A. C., Calitz, J. J., et al. 2002, arXiv Astrophysics e-prints, astro-ph/0207006

Bennett, D. P., Bhattacharya, A., Anderson, J., et al. 2015, ApJ, 808, 169

Bhattacharya, A., Beaulieu, J. P., Bennett, D. P., et al. 2018, AJ, 156, 289

Calchi Novati, S., Gould, A., Udalski, A., et al. 2015a, ApJ, 804, 20

Calchi Novati, S., Gould, A., Yee, J. C., et al. 2015b, ApJ, 814, 92

Calchi Novati, S., Skowron, J., Jung, Y. K., et al. 2018, AJ, 155, 261

Calchi Novati, S., Suzuki, D., Udalski, A., et al. 2019, AJ, 157, 121

Cardelli, J. A., Clayton, G. C., & Mathis, J. S. 1989, ApJ, 345, 245

DePoy, D. L., Atwood, B., Belville, S. R., et al. 2003, in Proc. SPIE, Vol. 4841, Instrument Design and Performance for Optical/Infrared Ground-based Telescopes, ed. M. Iye & A. F. M. Moorwood, 827–838

Dong, S., Carey, S., Gould, A., & Zhu, W. 2017, First Mass Measurement of a 'Domestic' Microlens, Spitzer Proposal, ,

Dong, S., Udalski, A., Gould, A., et al. 2007, ApJ, 664, 862

Dong, S., Gould, A., Udalski, A., et al. 2009, ApJ, 695, 970

Dong, S., Mérand, A., Delplancke-Ströbele, F., et al. 2019, ApJ, 871, 70

Fukui, A., Suzuki, D., Koshimoto, N., et al. 2019, arXiv e-prints, arXiv:1909.11802

Gaia Collaboration, Brown, A. G. A., Vallenari, A., et al. 2018, A&A, 616, A1

Gaudi, B. S. 2012, ARA&A, 50, 411

Gould, A. 1992, ApJ, 392, 442

—. 1994, ApJL, 421, L75

—. 1995, ApJL, 441, L21

—. 2000a, ApJ, 542, 785

—. 2000b, ApJ, 535, 928

—. 2004, ApJ, 606, 319

—. 2019, JKAS, 52, 121

Gould, A., Carey, S., & Yee, J. 2013, Spitzer Microlens Planets and Parallaxes, Spitzer Proposal, ,

—. 2014, Galactic Distribution of Planets from Spitzer Microlens Parallaxes, Spitzer Proposal, ,

—. 2016, Galactic Distribution of Planets Spitzer Microlens Parallaxes, Spitzer Proposal, ,

Gould, A., & Loeb, A. 1992, ApJ, 396, 104

Gould, A., Yee, J., & Carey, S. 2015a, Degeneracy Breaking for K2 Microlens Parallaxes, Spitzer Proposal, ,

—. 2015b, Galactic Distribution of Planets From High-Magnification Microlensing Events, Spitzer Proposal, ,

Gould, A., Yee, J., Carey, S., & Shvartzvald, Y. 2018, The Galactic Distribution of Planets via Spitzer Microlensing Parallax, Spitzer Proposal, ,

Gould, A., Udalski, A., Monard, B., et al. 2009, ApJL, 698, L147

Gould, A., Ryu, Y.-H., Calchi Novati, S., et al. 2019, arXiv e-prints, arXiv:1906.11183

Han, C., Bond, I. A., Gould, A., et al. 2018, AJ, 156, 226

Han, C., Yee, J. C., Udalski, A., et al. 2019, AJ, 158, 102

Hardy, S. J., & Walker, M. A. 1995, MNRAS, 276, L79

Holz, D. E., & Wald, R. M. 1996, ApJ, 471, 64

Jiang, G., DePoy, D. L., Gal-Yam, A., et al. 2004, ApJ, 617, 1307

Jung, Y. K., Han, C., Udalski, A., et al. 2018, ApJ, 863, 22

Jung, Y. K., Gould, A., Udalski, A., et al. 2019, AJ, 158, 28

Kennedy, G. M., & Kenyon, S. J. 2008, ApJ, 673, 502

Koshimoto, N., Shvartzvald, Y., Bennett, D. P., et al. 2017a, AJ, 154, 3

Koshimoto, N., Udalski, A., Beaulieu, J. P., et al. 2017b, AJ, 153, 1

Mao, S. 2012, Research in Astronomy and Astrophysics, 12, 947

Mao, S., & Paczynski, B. 1991, ApJL, 374, L37

Mao, S., Smith, M. C., Woźniak, P., et al. 2002, MNRAS, 329, 349

Mróz, P., Udalski, A., Skowron, J., et al. 2017, Nature, 548, 183

Mróz, P., Ryu, Y.-H., Skowron, J., et al. 2018, AJ, 155, 121

Mróz, P., Udalski, A., Bennett, D. P., et al. 2019, A&A, 622, A201

Nemiroff, R. J., & Wickramasinghe, W. A. D. T. 1994, ApJL, 424, L21

Nucita, A. A., Licchelli, D., De Paolis, F., et al. 2018, MNRAS, 476, 2962

Paczyński, B. 1986, ApJ, 304, 1

Poindexter, S., Afonso, C., Bennett, D. P., et al. 2005, ApJ, 633, 914

Refsdal, S. 1966, MNRAS, 134, 315

Ryu, Y.-H., Yee, J. C., Udalski, A., et al. 2018, AJ, 155, 40

Shappee, B. J., Prieto, J. L., Grupe, D., et al. 2014, ApJ, 788, 48

Shvartzvald, Y., Yee, J. C., Calchi Novati, S., et al. 2017, ApJL, 840, L3

Shvartzvald, Y., Yee, J. C., Skowron, J., et al. 2019, AJ, 157, 106

Street, R. A., Udalski, A., Calchi Novati, S., et al. 2016, ApJ, 819, 93

Sumi, T., Kamiya, K., Bennett, D. P., et al. 2011, Nature, 473, 349

Udalski, A., Yee, J. C., Gould, A., et al. 2015, ApJ, 799, 237

Udalski, A., Ryu, Y.-H., Sajadian, S., et al. 2018, AcA, 68, 1

Witt, H. J., & Mao, S. 1994, ApJ, 430, 505

Wyrzykowski, Ł., Kostrzewa-Rutkowska, Z., Skowron, J., et al. 2016, MNRAS, 458, 3012

Yee, J. C. 2015, ApJL, 814, L11

Yee, J. C., Udalski, A., Sumi, T., et al. 2009, ApJ, 703, 2082

Yoo, J., DePoy, D. L., Gal-Yam, A., et al. 2004, ApJ, 603, 139

Zang, W., Shvartzvald, Y., Wang, T., et al. 2019, arXiv e-prints, arXiv:1904.11204

Zhu, W., Calchi Novati, S., Gould, A., et al. 2016, ApJ, 825, 60

Zhu, W., Udalski, A., Huang, C. X., et al. 2017a, ApJL, 849, L31

Zhu, W., Udalski, A., Calchi Novati, S., et al. 2017b, AJ, 154, 210

Table 2. Best-fit parameters and their 68% uncertainty range from MCMC for the $u_{0,\oplus} > 0$ solutions

Parameters	$u_{0,\oplus} > 0$				
	non-parallax	w/o *Spitzer*	w/ *Spitzer*	VLTI + *Spitzer* (w/o lens light)	VLTI + *Spitzer* (w/ lens light)
$t_{0,\oplus}$ (HJD$'$)	8058.76(1)	8058.76(1)	8058.76(1)	8058.76(1)	8058.76(1)
$u_{0,\oplus}$	0.083(1)	0.084(1)	0.084(1)	0.085(1)	0.084(1)
$t_{\rm E}$	28.25(15)	27.98(42)	27.89(32)	27.83(15)	27.89(15)
$\pi_{\rm E,N}$	-	0.11(83)	0.68(56)	$-0.435(56)$	$-0.430(55)$
$\pi_{\rm E,E}$	-	0.06(13)	0.01(11)	0.193(24)	0.186(24)
$\pi_{\rm E}$	-	0.13(47)	0.68(23)	0.476(61)	0.469(60)
$V_{\rm CTIO,S}$	14.18(1)	14.17(2)	14.17(2)	14.15(1)	14.16(1)
$V_{\rm CTIO,B}$	17.17(10)	17.38(32)	17.36(27)	17.58(16)	17.55(15)
$H_{\rm CTIO,S}$	12.04(1)	12.03(2)	12.03(2)	12.02(1)	12.02(1)
$H_{\rm CTIO,B}$	13.69(3)	13.74(8)	13.74(7)	13.79(3)	13.78(3)
$\chi^2_{\rm Color}$	-	-	0.040	0.002	0.047
$\chi^2_{\rm VLTI}$	-	-	-	0.014	0.003
$\chi^2_{\rm total}/dof$	557.82/558	556.9/556	576.2/575	576.7/575	576.6/575

Table 3. Best-fit parameters and their 68% uncertainty range from MCMC for the $u_{0,\oplus} < 0$ solutions

Parameters	$u_{0,\oplus} < 0$				
	non-parallax	w/o *Spitzer*	w/ *Spitzer*	VLTI + *Spitzer* (w/o lens light)	VLTI + *Spitzer* (w/ lens light)
$t_{0,\oplus}$ (HJD$'$)	8058.76(1)	8058.76(1)	8058.76(1)	8058.76(1)	8058.76(1)
$u_{0,\oplus}$	-0.083	$-0.084(1)$	$-0.084(1)$	$-0.084(1)$	$-0.082(1)$
$t_{\rm E}$	28.26(16)	28.11(45)	28.24(38)	28.06(35)	28.15(29)
$\pi_{\rm E,N}$	-	0.67(81)	1.01(63)	$-0.003(234)$	$-0.003(223)$
$\pi_{\rm E,E}$	-	$-0.01(16)$	$-0.07(13)$	$-0.001(50)$	$-0.001(51)$
$\pi_{\rm E}$	-	0.67(52)	1.01(34)	0.003(239)	0.003(229)
$V_{\rm CTIO,S}$	14.18(1)	14.16(2)	14.17(2)	14.17(1)	14.17(1)
$V_{\rm CTIO,B}$	17.17(10)	17.40(34)	17.33(29)	17.27(27)	17.22(23)
$H_{\rm CTIO,S}$	12.04(1)	12.02(2)	12.03(2)	12.03(1)	12.04(1)
$H_{\rm CTIO,B}$	13.69(3)	13.75(8)	13.73(7)	13.71(6)	13.70(6)
$\chi^2_{\rm Color}$	-	-	0.002	39.840	40.728
$\chi^2_{\rm VLTI}$	-	-	-	0.033	0.009
$\chi^2_{\rm total}/dof$	557.83/558	556.7/556	576.2/575	618.2/575	618.0/575

Table 4. Blend from the best-fit "luminous lens" model versus the predicted apparent magnitude of the lens

Band	H	I	R	V
Extinction A_λ	0.10	0.42	0.66	0.87
Blending	13.78 ± 0.03	16.30 ± 0.07	16.76 ± 0.10	17.55 ± 0.15
Predicted lens apparent magnitude	13.9 ± 0.3	16.2 ± 0.4	16.7 ± 0.6	17.6 ± 0.8

Table 5. Physical parameters for the lens of TCP J0507+2447

$M_{\mathrm{L}}\ [M_{\odot}]$	0.495 ± 0.063
$D_{\mathrm{L}}\ [\mathrm{pc}]$	429 ± 21
$D_{\mathrm{S}}\ [\mathrm{pc}]$	692 ± 15
$\mu_{\mathrm{L,hel,N}}\ [\mathrm{mas\,yr^{-1}}]$	28.89 ± 0.41
$\mu_{\mathrm{L,hel,S}}\ [\mathrm{mas\,yr^{-1}}]$	13.39 ± 0.61
$\mu_{\mathrm{S,hel,N}}\ [\mathrm{mas\,yr^{-1}}]$	-6.42 ± 0.36
$\mu_{\mathrm{S,hel,S}}\ [\mathrm{mas\,yr^{-1}}]$	-0.80 ± 0.23
$\mu_{\mathrm{rel,hel,N}}\ [\mathrm{mas\,yr^{-1}}]$	-22.45 ± 0.21
$\mu_{\mathrm{rel,hel,E}}\ [\mathrm{mas\,yr^{-1}}]$	14.18 ± 0.59
$\mu_{\mathrm{rel,geo,N}}\ [\mathrm{mas\,yr^{-1}}]$	-22.73 ± 0.21
$\mu_{\mathrm{rel,geo,E}}\ [\mathrm{mas\,yr^{-1}}]$	9.83 ± 0.19

Table 6. Binary-lens fitting results with the VLTI constraints

| Parameters	$s = 0.935$				$s = 0.975$			
	$u_{0,\oplus} > 0$		$u_{0,\oplus} < 0$		$u_{0,\oplus} > 0$		$u_{0,\oplus} < 0$	
	w/o lens light	w/ lens light	w/o lens light	w/ lens light	w/o lens light	w/ lens light	w/o lens light	w/ lens light
$t_{0,\oplus}$ (HJD$'$)	8058.76(1)	8058.76(1)	8058.76(1)	8058.76(1)	8058.76(1)	8058.76(1)	8058.78(1)	8058.76(1)
$u_{0,\oplus}$	0.086(1)	0.086(1)	$-0.094(1)$	$-0.086(3)$	0.086(1)	0.086(1)	-0.079	-0.084
t_{E}	27.82(16)	27.82(16)	28.10(41)	28.04(67)	27.81(17)	27.84(16)	29.61(48)	28.15(37)
$q(10^{-4})$	1.1	1.1	1.1	1.1	1.1	1.1	1.1	1.1
α (rad)	1.625	1.625	4.658	4.658	1.516	1.516	4.767	4.767
$\rho(10^{-3})$	5.5(6)	5.5(6)	81(16)	5.6(8)	5.8(6)	6.1(6)	5.1(5)	6.1(6)
$\pi_{\mathrm{E,N}}$	$-0.427(57)$	$-0.433(56)$	$-0.014(337)$	$-0.023(435)$	$-0.445(56)$	$-0.432(58)$	$-0.004(292)$	$-0.004(287)$
$\pi_{\mathrm{E,E}}$	0.189(25)	0.188(23)	$-0.003(76)$	$-0.006(102)$	0.197(24)	0.186(25)	$-0.001(66)$	$-0.001(65)$
π_{E}	0.467(62)	0.472(61)	0.015(346)	0.024(447)	0.486(61)	0.470(63)	0.004(299)	0.004(295)
$V_{\mathrm{CTIO,S}}$	14.15(1)	14.15(1)	14.17(2)	14.16(3)	14.15(1)	14.15(1)	14.17(3)	14.17(3)
$V_{\mathrm{CTIO,B}}$	17.71(20)	17.68(19)	17.38(41)	17.39(62)	17.70(20)	17.71(20)	17.29(52)	17.28(53)
$H_{\mathrm{CTIO,S}}$	12.02(1)	12.02(1)	12.03(2)	12.03(3)	12.02(1)	12.02(1)	12.03(3)	12.03(3)
$H_{\mathrm{CTIO,B}}$	13.81(4)	13.81(4)	13.74(10)	13.74(14)	13.81(4)	13.81(4)	13.72(13)	13.71(13)
χ^2_{Color}	0.026	0.019	41.722	41.891	0.027	0.058	41.643	41.274
χ^2_{VLTI}	0.040	0.114	0.074	0.028	0.024	0.026	0.202	0.390
$\chi^2_{\mathrm{total}}/dof$	575.1/554	575.2/554	618.9/574	619.0/574	575.3/574	575.2/574	617.8/574	617.2/574
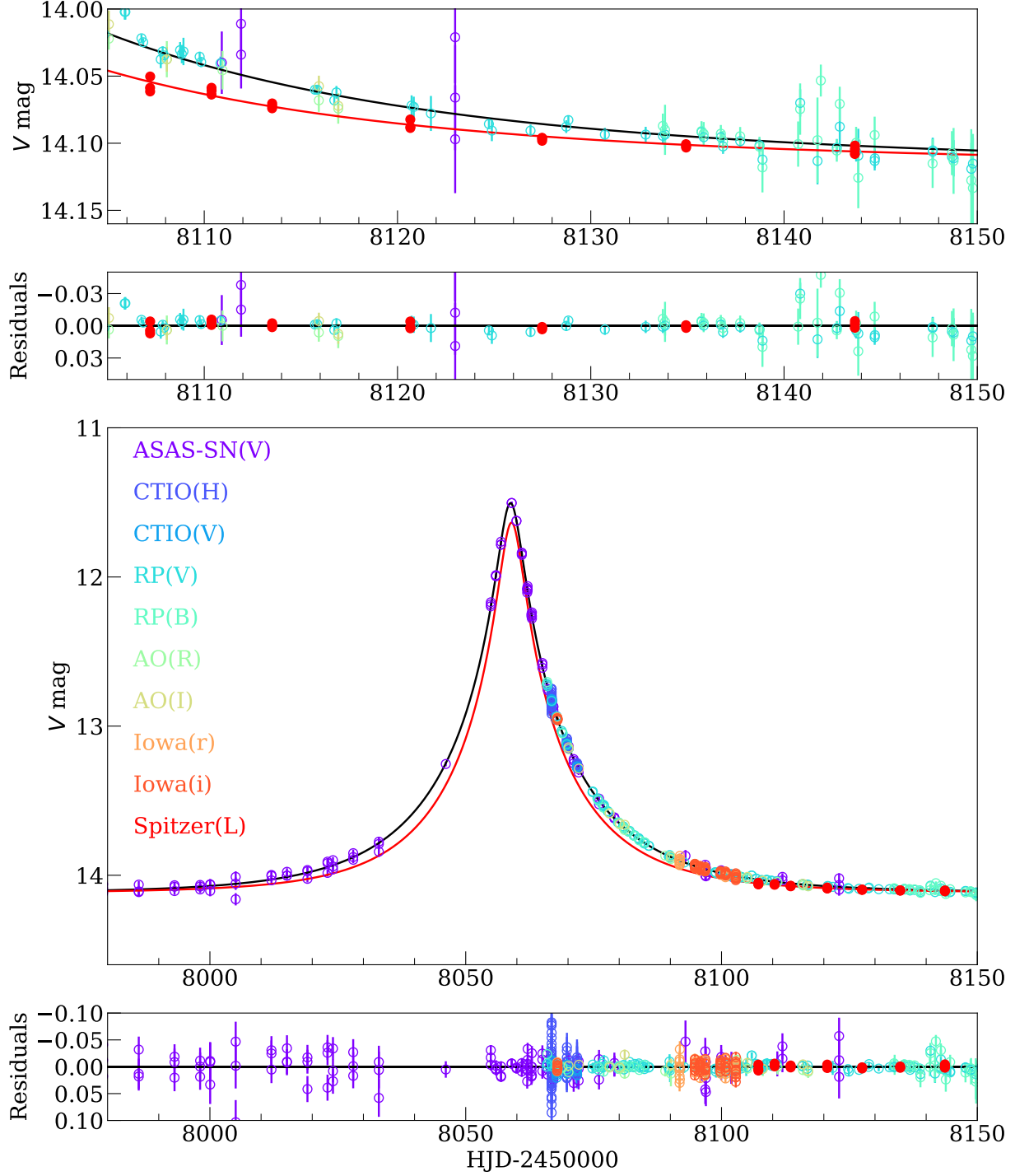
Figure 1. The light curves and data points of TCP J0507+2447. The upper panel show a close-up of *Spitzer* data points. The black line represent the best-fit $u_{0,\oplus} > 0$ with lens light model for the ground data, and the red line shows the corresponding model for *Spitzer*. The circles with different colors are ground-based data points from different telescopes or bands. The red dots are *Spitzer* data points.
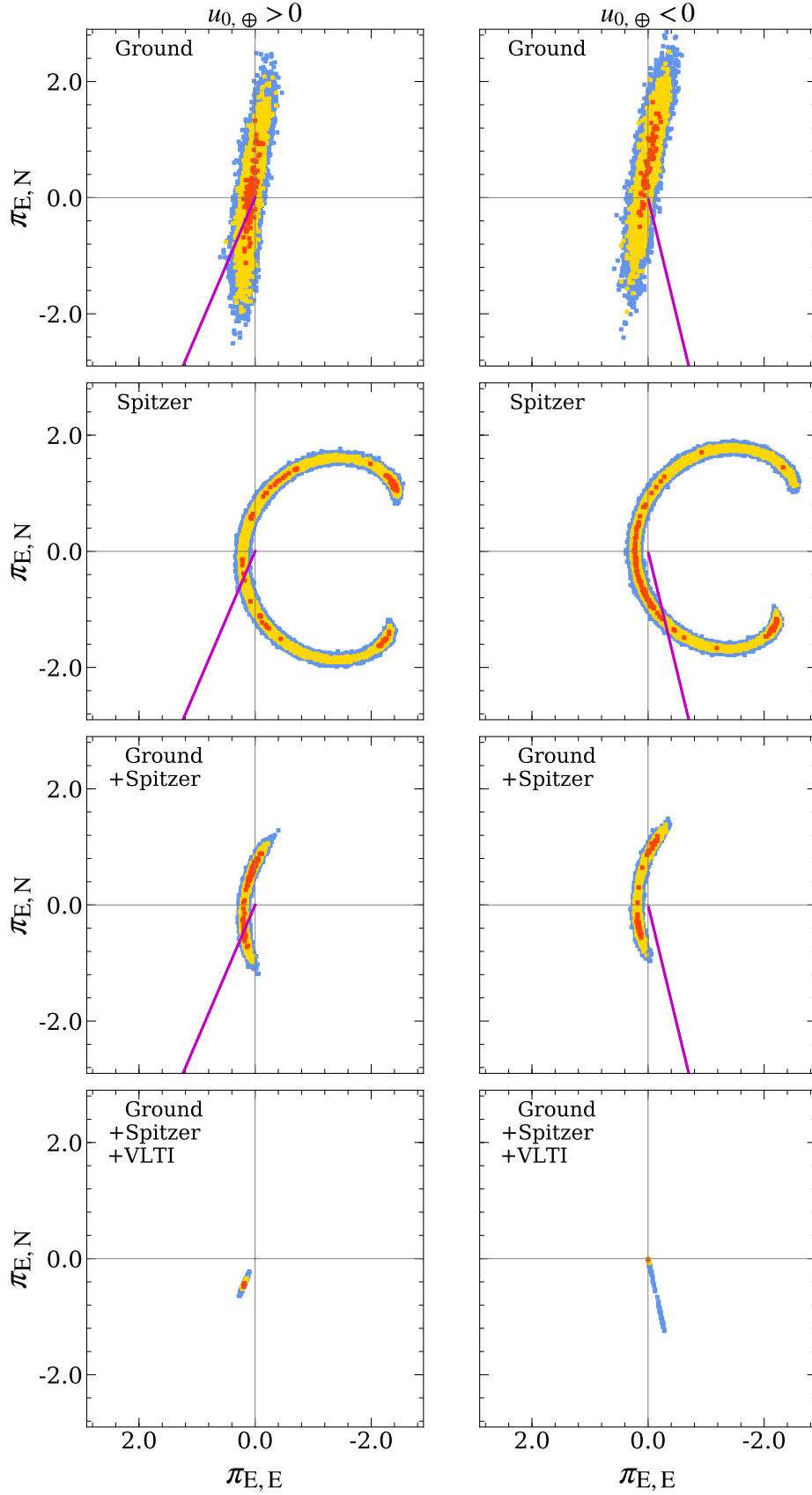
Figure 2. Likelihood distributions for π_E derived from MCMC. The left and right panels show the distributions for $u_0 > 0$ and $u_0 < 0$ solutions, respectively. Red, yellow, and blue show likelihood ratios $[-2\Delta \ln \mathcal{L}/\mathcal{L}_{max}] < (1, 4, \infty)$, respectively. The magenta lines represent the best value of the VLTI directions.
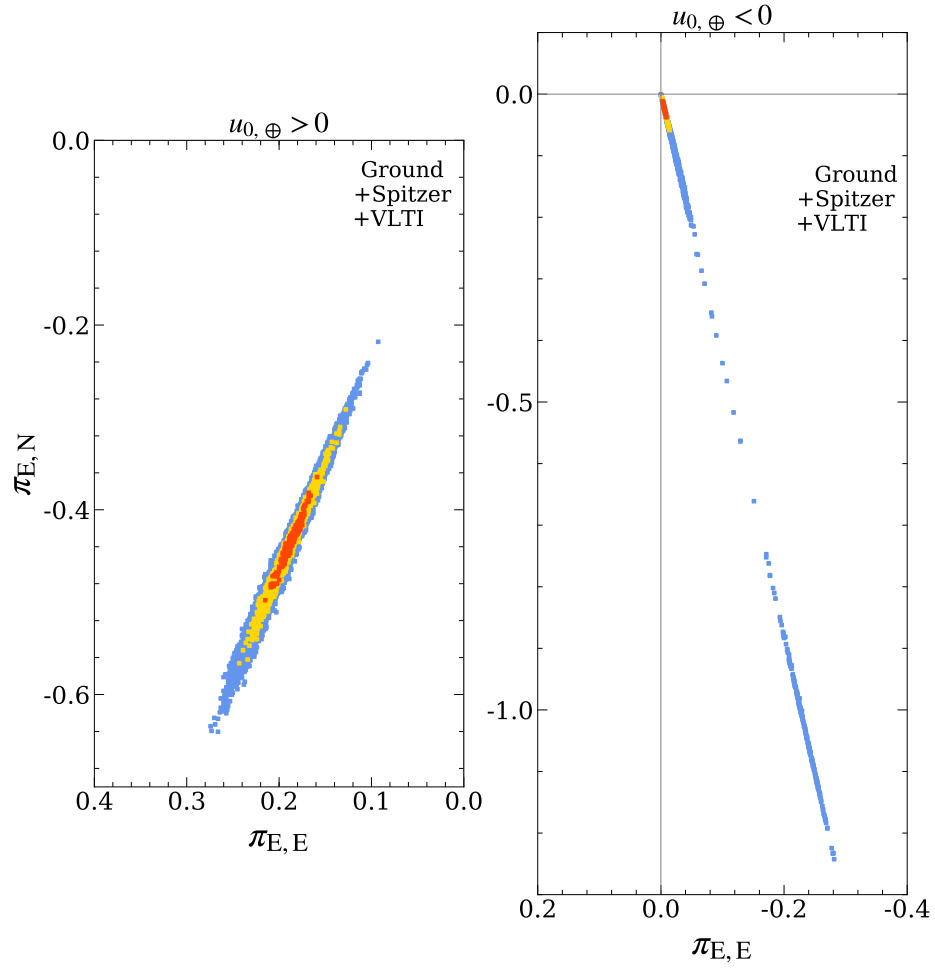
Figure 3. The Close-up of $\pi_\mathbf{E}$ Likelihood distributions with Ground + *Spitzer* + VLTI constraints. The symbols are similar to those in Figure 2.